Available online at www.sciencedirect.com
ScienceDirect
Acta Materialia 57 (2009) 5882–5891
Acta MATERIALIA
www.elsevier.com/locate/actamat

Energetics of charged point defects in rutile TiO_2 by density functional theory

X. Li [a], M.W. Finnis [c], J. He [b], R.K. Behera [b], S.R. Phillpot [b], S.B. Sinnott [b], E.C. Dickey [a,*]

[a] Department of Materials Science and Engineering, Pennsylvania State University, University Park, PA 16802, USA
[b] Department of Materials Science and Engineering, University of Florida, Gainesville, FL 32611, USA
[c] Department of Materials, Imperial College London, Exhibition Road, London SW7 2AZ, UK

Received 1 May 2009; received in revised form 5 August 2009; accepted 7 August 2009
Available online 16 September 2009

Abstract

The defect formation energies of all possible charge states of point defects in TiO_2, including titanium interstitials, titanium vacancies and oxygen vacancies, are calculated in the phase space of temperature, oxygen partial pressure and Fermi level by combining density functional theory (DFT) and thermodynamic calculations. The point defect phase diagram illustrates that fully charged defects dominate in most regimes. The calculations not only give reasonable defect formation energies compared with prior experimental measurements, but also predict n-type TiO_2 at high T and low P_{O_2}, and p-type TiO_2 at low T and high P_{O_2}, which agrees well with experimental data. In addition, we evaluate methods for correcting the effects of artificial electrostatic interactions caused by periodic boundary conditions in the DFT calculations, including the electrostatic potential alignment correction (ΔV correction) and the Makov–Payne correction.

Keywords: DFT; Artificial electrostatic correction; Thermodynamics; Charged point defect

1. Introduction

Charged point defects in TiO_2 are largely responsible for its electrical properties, which have been measured experimentally by several groups [1–5]. Nonetheless, controversies remain about the dominant point defects responsible for the conductivity behavior in certain temperatures and oxygen partial pressure (P_{O_2}) ranges. At temperatures above 1700 K and in the reduced P_{O_2} regime (10^{-11}–10^{0} atm) it is widely accepted that fully charged titanium interstitials (Ti_i^{4+} in Kröger–Vink notation) are the dominant defects [3]. At intermediate temperatures, however, there are more discrepancies in the data. For example, at around 1300 K the electrical conductivity measurements of Baumard et al. [1] indicate that fully charged Ti interstitials, Ti_i^{4+}, are dominant, while Blumenth et al. [5] found that Ti_i^{3+} dominates in the low P_{O_2} range. In addition, Balachandran and Eror [6] found that fully charged oxygen vacancies, V_O^{2+}, dominate at low P_{O_2} while at intermediate P_{O_2} impurities may play a role in their samples. More recent studies by Lee and Yoo [7] claim that Ti_i^{3+}, Ti_i^{4+}, and V_O^{2+} successively dominate as P_{O_2} increases, while Nowotny et al. [3] claim that V_O^{2+} dominates at low P_{O_2}, while at intermediate P_{O_2}, both V_O^{2+} and V_{Ti}^{4-} are dominant. These discrepancies in the literature could arise from different impurity levels or incomplete equilibration of the samples in some cases. Regardless of their origin, however, they emphasize the need to understand point defect thermodynamics from a more fundamental, theoretical perspective.

Density functional theory (DFT) within the supercell approximation is widely used to calculate point defect formation energies (DFEs) that are not accessible experimentally and to provide a theoretical understanding of experimentally observed properties [8,9]. Recently, DFT calculations of the neutral titanium interstitial (Ti_i^0) and oxygen vacancy (V_O^0) in rutile TiO_2 by Cho et al. [10] analyzed the charge localization around the defects, and

* Corresponding author.
E-mail address: ecd10@psu.edu (E.C. Dickey).

1359-6454/$36.00
doi:10.1016/j.actamat.2009.08.014

showed that two of the $3d^24s^2$ electrons of the titanium interstitial are localized at the defect site while the other two are delocalized. Charged defects are simulated in the DFT scheme by adding or removing electrons from the defective supercells with a compensating uniform background. Charged defects in TiO_2 were calculated by He et al. [11] by combining DFT with thermodynamics to predict the defect formation energies as a function of temperature, oxygen partial pressure and Fermi level.[1] These DFT calculations were carried out with relatively small $2 \times 2 \times 3$ supercells. When charged point defects are examined in DFT calculations, the artificial electrostatic interactions between point defects in neighboring supercells, which arise from the periodic boundary conditions, must be taken into account. The Makov–Payne correction [12] and its first-order approximation of the Leslie and Gillan correction [13] have been used to correct the artificial interactions by treating the charges as localized multipoles [11].

Here, we investigate how localized the excess charge actually is by applying an atom-by-atom Bader analysis to the charge density around the region of a defect, with reference to the perfect crystal. This is a new approach in the present context, and we describe it in detail in Section 3.1. It provides complementary information to the qualitative localization analysis of the density of states of neutral defective supercell by Cho et al. [10]. The physical significance of the charge localization and its influence on the application of Makov–Payne correction is analyzed by comparing the supercells of various sizes up to $3 \times 3 \times 5$ TiO_2 unit cells in Section 3.2. We also evaluate the effectiveness of the so-called ΔV correction method [14,15] in Section 3.2, which we ultimately find to be a better correction scheme for this system in that it is more efficient at converging the defect formation energies as a function of supercell size. The defect formation energies determined using the ΔV correction are then used in a thermodynamic framework in Section 4 to provide improved point defect phase diagrams relative to the previous work [11].

2. Calculation method

In this work, DFT calculations are carried out using the Vienna Ab-initio Simulation Package (VASP) [16,17]. The calculations use the generalized gradient approximation Perdew–Burke–Ernzerhof (GGA-PBE) [18] exchange–correlation functionals to obtain the ground-state energies of the supercells. Projector augmented wave (PAW) pseudopotentials [17,19] that explicitly calculate the $3s^23p^63d^24s^2$ electrons for titanium and the $2s^22p^4$ electrons for oxygen are used for all calculations. The cutoff-energy of 354 eV and k-points sampling of $4 \times 4 \times 4$ are determined after careful tests for convergence. The total-energy and residual-force convergence criteria are set to 10^{-4} eV and 0.01 eV $Å^{-1}$, respectively. The calculated lattice parameters of the defect-free unit cell are listed in Table 1, and these are then used to build the supercell.

Supercell size convergence is an important issue for charged point defect calculations with periodic boundary conditions. We assess finite-size effects arising from electrostatic interactions between a charged defect and its periodic images through the valence-band offset, or ΔV, correction [14] and the Makov–Payne approach [12,13]. In our calculations, defective supercells of various sizes from $2 \times 2 \times 2$ to $3 \times 3 \times 5$ TiO_2 unit cells are examined to evaluate the convergence with increasing supercell size of the DFEs, charge density distribution, external pressure and correction energies. We finally adopt a protocol for obtaining accurate defect formation energies in the TiO_2 system, namely to use as large a supercell as possible (in this case $3 \times 3 \times 5$ unit cells) and to apply the ΔV correction.

The method of combining DFT with thermodynamics [11] is based on the widely used formula for calculating DFEs [9,20,21]:

$$\Delta G_\alpha = E_\alpha - E_{perfect} + n_a\mu_a(T, P_{O_2}) + q_\alpha(E_F + E_{VBM}) + \text{correction}. \quad (1)$$

The chemical potential of element a, $\mu_a\,(T, P_{O_2})$ can be divided into several sub-terms that can be either calculated by ab initio methods or measured experimentally with specified temperature and oxygen partial pressure dependence. In Eq. (1) ΔG_α, the defect formation energy of defect species α, includes the difference between the total-energy of the defective supercell, E_α, and the energy of the perfect supercell, $E_{perfect}$ The term n_a, $\mu_a\,(T, P_O)$ balances the number of atoms in the formula for the formation of the point defect; n_a is -1 for an interstitial and $+1$ for a vacancy. Similarly the $q_\alpha(E_F + E_{VBM})$ term balances the number of electrons involved in the formation of the charged defects, where q_α is the charge state of the defect, E_{VBM} is the valence-band maximum (VBM) referenced to the DFT zero of energy in the ab initio calculation, and E_F is the Fermi level in the material with respect to the E_{VBM}. The last correction term accounts for the artificial electrostatic interaction between defect images in the charged supercell caused by the periodic boundary conditions; this will be discussed in detail below.

The chemical potential term is calculated in the binary system of TiO_2 for $a = O$ as:

Table 1
Lattice parameter calculated from DFT compared with experiments.

	a (Å)	c (Å)
Experiment	4.59	2.96
GGA-PBE	4.65	2.97
	+1.3%	+0.3%

[1] Note that there was a systematic error to the Makov–Payne correction in Ref. [11] which did not include the $1/4\pi$ factor in the $q^2\alpha_M/4\pi\varepsilon\varepsilon_0 r$ monopole correction, and hence overestimated the Makov-Payne correction by an order of magnitude. Its influence on the final results is discussed in Section 3.

$$\mu_O = \mu_O^0 + \Delta\mu_O^0(T) + \frac{1}{2}k_B T \ln\left(\frac{P_{O_2}}{P^0}\right) = \frac{1}{2}(\mu_{TiO_2}^0 - \mu_{Ti}^0 - \Delta G_{f,TiO_2}^0) + \Delta\mu_O^0(T) + \frac{1}{2}k_B T \ln\left(\frac{P_{O_2}}{P^0}\right), \quad (2)$$

which was originally applied to the Al_2O_3 system by Finnis and coworkers [22,23]. It is important to note [24] that there is a lower bound for μ_O below which the TiO_2 compound will discompose into oxygen and titanium, and our calculations are within that limit.

When $a = \mathrm{Ti}$:

$$\mu_{Ti}(T, P_{O_2}) = \mu_{TiO_2}^0 - 2\mu_O(T, P_{O_2}). \quad (3)$$

In the above two equations the standard chemical potential of a Ti atom, μ_{Ti}^0, and rutile TiO_2 molecular unit, $\mu_{TiO_2}^0$, are estimated by DFT calculations at 0 K. The temperature-dependent part of the chemical potential of oxygen at standard pressure, $\Delta\mu_O^0(T)$, and the standard formation energy, $\Delta G_{f,TiO_2}^0$ are taken from the NIST thermodynamic experimental database [25]. As pointed out by Finnis et al. [26], the standard chemical potentials for TiO_2 and Ti calculated at 0 K by DFT are adequate estimates for the standard temperature and pressure because rutile TiO_2 and metallic Ti are solids. With this approach, the DFEs at high temperature, different oxygen partial pressure and Fermi level can be calculated on an ab initio basis.

3. Results and discussion

3.1. Charge localization and ionic displacement analysis

Our aim in this section is to give a quantitative procedure for defining the spatial distribution of the Kröger–Vink charge of a defect, a matter that is by no means trivial because the lattice around the defect is discrete, strained and polarized, all of which make it problematic simply to integrate the charge over a region around the defect. For any defective supercell, such as Ti_i^q, the charge state q is not defined without a clear statement of the reference state. In most cases, including the Kröger–Vink convention, the reference background is the perfect supercell. Thus it is the charge density difference between the defective and the perfect supercells that defines the charge associated with point defect Ti_i^q.

A point-by-point subtraction of the charge density of the perfect lattice from the charge density in the defective supercell will exhibit huge, spatially dependent oscillations due to the displacements of the nuclear positions around the defect, which carry with them a proportion of the electron density. Instead, we employ a course-graining, discretization procedure for the charge density, and map it onto individual ions. All the electronic charges are allocated to individual ions according to the Bader prescription [27], for both the defective and the perfect crystals. In order to define excess charge the subtraction is then done not point-by-point in space, but atom-by-atom, which gives the excess charge as a function of distance from the defect.

The Bader volume of each ion is defined by the surface around it whose normal points along the direction in which the surrounding charge density has zero gradient. These volumes fill the space of the supercell seamlessly without empty space or overlap. The integrations of all the electrons inside each unit region defined by the Bader volumes in a perfect supercell give a value of 7.1 electrons around each oxygen ion and 9.8 electrons around each titanium ion. In the perfect crystal this defines an ionic charge of −1.1 for the oxygen ion and +2.2 for the titanium ion, which agrees reasonably well with the experimental analysis of the charge state of a titanium ion in rutile TiO_2 [28], although we do not presume it to have any absolute physical meaning. They also agree well with the results of a simple analysis of the relationship between electronegativity and charge state [29], where the Pauling electronegativity difference between O of 3.5 and Ti of 1.6 [28] predicts a charge state of -1.1 for the O ion in TiO_2.

The number of electrons that belong to each Ti or O ion in the defective and perfect supercells can be obtained by integrating over the respective Bader volumes, and their difference is then calculated. Fig. 1 illustrates the average number of electron difference (dashed line) and average ionic displacement (solid line) per Ti or O ion inside the successive spherical shells around the Ti interstitial nucleus

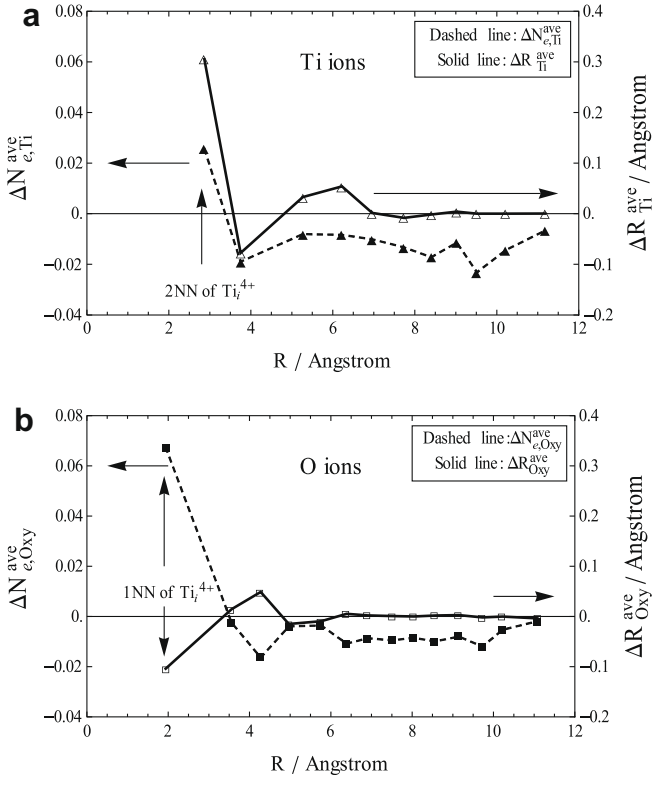

Fig. 1. Partial charge density difference (dashed line) (a) per Ti ion and (b) per O ion; and the average ion displacement (solid line) averaged over (a) Ti ion and (b) O ion inside each successive spherical shell within radius R and $R + \Delta R$ from the Ti_i^{4+} defect nucleus in the $3 \times 3 \times 5$ supercell.

as a function of distance R from the defect. The thickness of each spherical shell is chosen based on the criterion that the distance between any two ions is always less than 0.5 Å within each shell. The choice of other values for this criterion should not influence our major conclusion. However, too small a value might introduce noise, while too large a value might hide the useful details. The calculation shows that the first nearest neighbor (1NN) O ions in Fig. 1b and second nearest neighbor (2NN) Ti ions in Fig. 1a of the Ti interstitials all have positive electron differences, which is due to the partial transfer of charge from these neighbors to the interstitial or further regions. Beyond the 2NN shell, the charge transfer fluctuates all the way to the edge of the supercell, which may be indicative of the propensity of DFT to favor delocalized electron states [10,30]. Comparison of Fig. 1a and b indicates that for titanium ions the relaxations toward the titanium interstitial are mostly accompanied with a loss of electrons within their Bader volumes, and the relaxations away from the defect nucleus are associated with gain in local electron density; while for oxygen ions the opposite trend is implied. This is as one would expect if the relaxations are driven by the electrostatic interactions of the ions. The ionic displacements in the defective supercell are found to converge to the perfect crystal values more quickly with increasing distance from the defect site than the charge density.

We now examine in more detail the spatial extent of the defect charge density. Fig. 2a shows the total charge density difference oscillation as a function of distance from the defect nucleus for differently charged Ti_i^q supercells at two different sizes. The excess charge on the nearest neighbors of the interstitial atom is surprisingly insensitive to the charge in the supercell. We see in the smaller supercell that the average charge carried by the nearest neighbors varies in the range -0.1 to -0.03 while the charge in the supercell varies over the whole range from 0 to $+4$. In the larger supercell, where the excess charge has more room to spread, the variation in charge localized on the nearest neighbors is even less. The charge densities also oscillate with much higher amplitudes as a function of distance from the interstitial in $2 \times 2 \times 3$ supercells compared with the $3 \times 3 \times 5$ supercells. By summing the electron difference within each discrete radius, the total electron difference around the defect nucleus can be plotted as a function of distance from the defect nucleus, as shown in Fig. 2b for the same set of charged Ti_i^q supercells of two different sizes. The values for the interstitial itself $\sum \Delta N_e(R=0)$ are all close to 10 regardless of the charge of the overall supercell. A neutral interstitial would have a value $\Delta N_e^{tot} = 12$, which shows that the charge states within the Bader volumes of the titanium interstitial at $R=0$ are always around $+2$ for all differently charged Ti_i^q supercells, just as they are for Ti lattice sites in the perfect crystal. This result is consistent with the new model of the charge self-regulation around a transition metal ion in semiconductors to make the local charge constant, no matter what the oxidation states are [31].

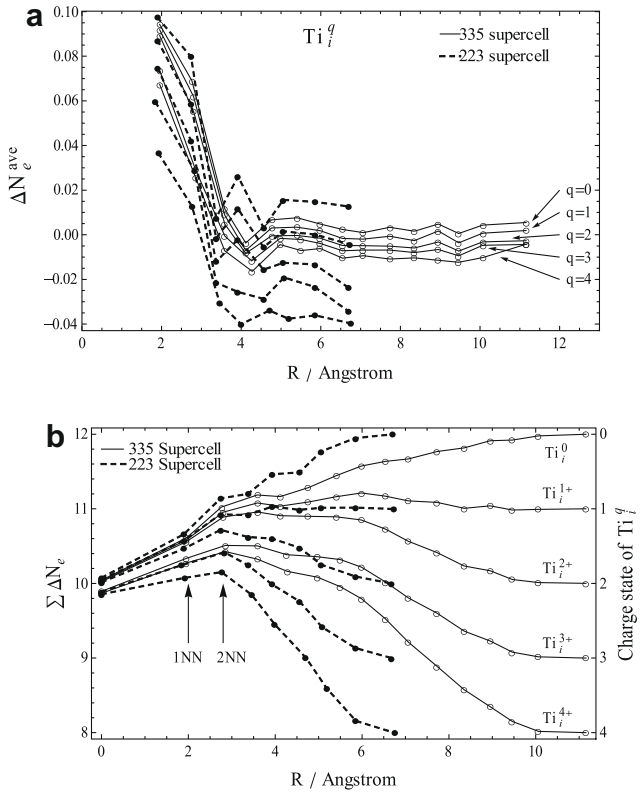

Fig. 2. (a) Total charge density difference (given as difference in number of electrons) averaged over all ions inside each successive spherical shell within radius R and $R+\Delta R$ from the defect nucleus for $2 \times 2 \times 3$ and $3 \times 3 \times 5$ sized for differently charged Ti_i^q supercells. (b) Cumulative electron difference within radius R around defect nucleus between Ti_i^q defective and perfect supercells.

For the Ti_i^{1+} supercell illustrated in Fig. 2b the excess charge has all been accommodated at the interstitial and its first and second neighbors, a region well within the faces of the supercell. In the other cases, it is clear that the size of the supercell is strongly affecting the charge distribution, because the excess charge density is varying right up to the faces of the supercell. In an infinitely large supercell the amplitude of the charge density oscillation would damp to zero at a certain distance. Within this range all the structural distortion and charge density difference oscillations are the intrinsic structures of the point defect, Ti_i^q, while from any viewpoint far beyond this range the charge state of this entity is always the nominal value q. However, our largest supercells are still too small to contain this range, except perhaps for the Ti_i^{1+} charged supercell.

3.2. Influence of defect charge distribution on choice of correction method

The intention of the Makov–Payne correction is to account for the artificial electrostatic interaction between the charged point defect images including the jellium background in the supercell because of the periodic boundary conditions [12]. Its first-order correction is identical to Leslie and Gillan's result [13], which was applied to charged

defects in TiO_2 in our earlier publication [11]. Our examination of the charge localization state range by the method of real-space charge integration in the previous section indicates that for the rutile TiO_2 the charge delocalization around the defect invalidates the application of the Makov–Payne correction. Furthermore, as pointed out by Castleton et al. [32], the DFT dielectric constant may not be the same as the experimental value because the dielectric constant is an intrinsically macroscopic quantity arising from an ensemble of ions; its application at this microscopic level is potentially problematic.

Promising new approaches for correcting the electrostatic interactions between supercells have been very recently proposed by Freysoldt et al. [33]; these make use of an analysis of electrostatics in dielectric media. However, here we find the simpler electrostatic potential alignment correction (ΔV correction) to be adequate for our rutile TiO_2 system in that it converges the DFEs very quickly. The ΔV correction takes into account the fact that the VBM in the neighborhood of a charged defect is shifted with respect to the perfect crystal, which generates the energy used to exchange the electrons between VBM and the Fermi level. The value of the valence-band shift is estimated from the difference between the average electrostatic potential at the edge of the defective supercell and the perfect supercell [14,20]. In view of the approximate nature of its derivation, we regard this ΔV correction as largely empirical.

Fig. 3 presents the DFEs for Ti_i^{4+} and V_{Ti}^{4-} as a function of supercell size with the two different corrections applied. The results indicate that the ΔV correction converges the total energies more rapidly with increasing supercell size than does the Makov–Payne correction. The corrected energies in Fig. 3 do not include the chemical potential and Fermi level terms in Eq. (1), since these terms do not affect the convergence analysis. Table 2 lists the values for the different correction methods and the final DFEs for $2 \times 2 \times 3$ and $3 \times 3 \times 5$ supercells. It is clear that, even including both first- and second-order terms, the Makov–Payne correction scheme does not converge as quickly as the ΔV correction for this system. For these reasons the following results consider only the ΔV correction.

3.3. Artificial elastic energy interaction

Although the correction methods mentioned above are widely used to correct for artificial electrostatic effects associated with the small system sizes, none explicitly includes a correction for the possible artificial elastic energy interactions inherent in the supercell approach. One possible scheme to account for this effect is to allow the supercell volume to relax in the DFT calculations such that the external pressure on the supercell after relaxation is close to zero; this simulates a physical scenario in which the physical defect concentration is the same as the (extremely high) defect concentration in the supercell. Another approach that is usually considered to be more appropriate

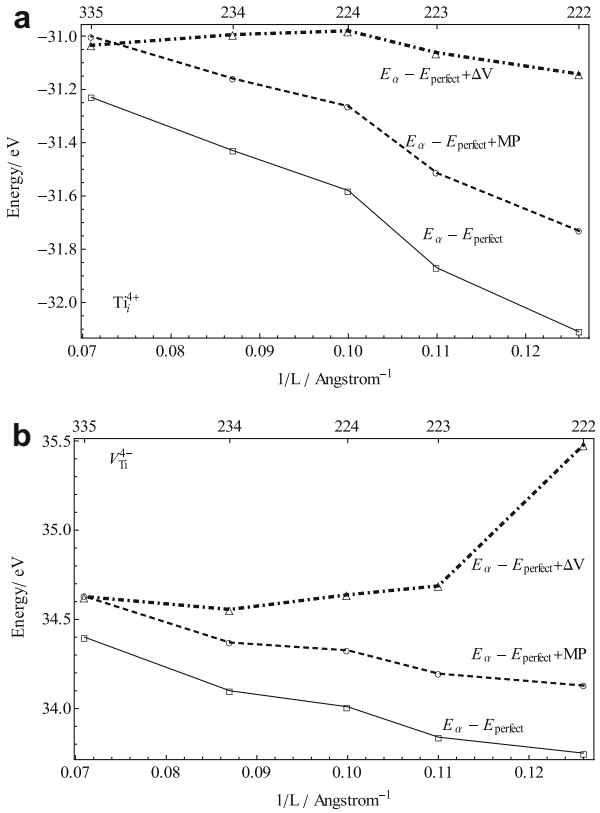

Fig. 3. The energy of $E_\alpha - E_{perfect}$ (solid line) for Ti_i^{4+} (a) and V_{Ti}^{4-} (b) after Makov–Payne correction (dashed line) and ΔV correction (dot-dashed line), respectively, as a function of the supercell sizes.

for the dilute solution approximation, which is of interest here, is to fix the supercell volume during the relaxation, such that the elastic strain field interacts with the boundary of the supercell and leaves an external pressure on the relaxed supercell.

The pressure on the supercells in the constant-volume method can be used to estimate its energy difference E_P from the corresponding zero-pressure supercell by the classical formula of elastic strain energy $\frac{1}{2}\frac{VP^2}{Y}$, where V is the volume of the supercell, P is the external pressure on the supercell using the constant-volume method from DFT calculation and Y the experimental bulk modulus of bulk rutile TiO_2 [34]. The calculated energy difference as a function of supercell size for five different defective supercells is shown in Fig. 4a. These values agree reasonably well with the energy differences taken directly from the DFT-calculated, zero-pressure supercell energies for several tested cases. The figure illustrates that the energy difference can be very large at small supercells: ~1 eV for the $2 \times 2 \times 3$ V_{Ti}^{4-} supercell, while at $3 \times 3 \times 5$ supercells the difference is ~0.1 eV. We can compare the convergence behavior of the two supercell boundary conditions by first calculating the DFEs in the constant volume approach, followed with the subtraction of the elastic strain energy term, E_P, to obtain the DFEs in the zero-pressure approach. We find that the constant-volume method converges more quickly than the zero-pressure method for highly charged

Table 2
DFE after different correction methods. The two MP(q) terms are the Makov–Payne 1st and 2nd order corrections by defining the point charges with different radii around the defects between 0.7 and 2 Å.

$[\alpha^q]$	ΔE	MP $(1/L,q)$	MP $(1/L^3,q)$	$q*\Delta V$	ΔE + MP $(1/L,1/L^3,q)$	$\Delta E + q*\Delta V$
Ti_i^{4+}_223	−31.87	0.251	0.099	0.808	−31.520	−31.062
Ti_i^{4+}_335	−31.23	0.162	0.070	0.196	−30.998	−31.034
Ti_i^{2+}_223	−20.78	0.063	0.019	0.454	−20.698	−20.326
Ti_i^{2+}_335	−20.47	0.040	0.016	0.108	−20.414	−20.362
V_{Ti}^{4-}_223	33.84	0.251	0.099	0.848	34.190	34.688
V_{Ti}^{4-}_335	34.40	0.162	0.070	0.228	34.632	34.628
V_{Ti}^{2-}_223	27.65	0.063	0.019	0.400	27.732	28.050
V_{Ti}^{2-}_335	27.70	0.040	0.015	0.114	27.755	27.814

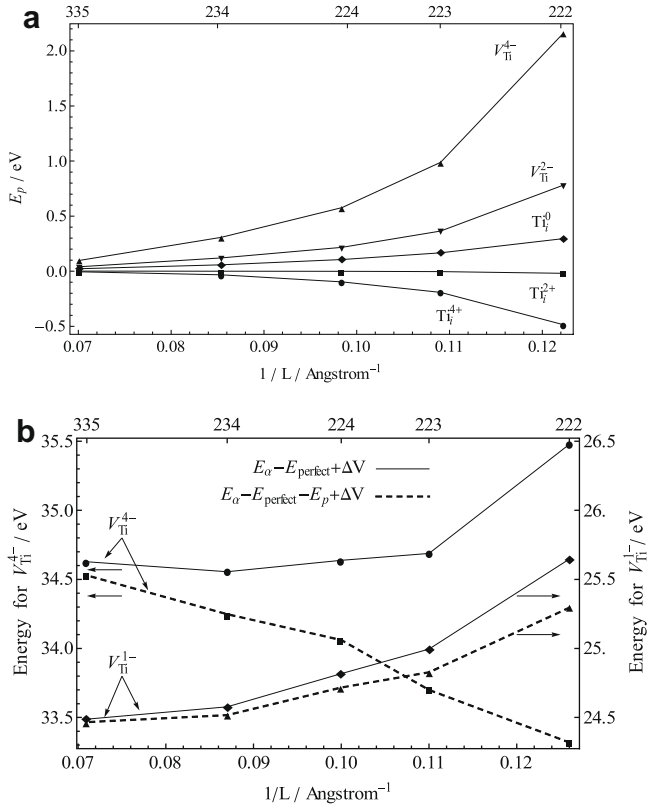

Fig. 4. (a) The elastic strain energies calculated from the external pressures on the constant volume supercells as a function supercell sizes, using formula $E_p = VP^2/2Y$. (b) Comparison of the convergence between the constant volume $(E_\alpha - E_{perfect})$ and zero-pressure method $(E_\alpha - E_{perfect} - E_P)$ after ΔV correction for V_{Ti}^{4-} and V_{Ti}^{1-} supercells.

supercells, i.e. Ti_i^{4+}, Ti_i^{3+}, V_{Ti}^{4-}, V_{Ti}^{3-} and V_O^{2+}. For intermediately charged supercells, i.e. Ti_i^{2+}, V_{Ti}^{2-} and V_O^{1+}, both methods have very similar convergence behaviors, while for the supercells with low charge states, i.e. Ti_i^{1+}, Ti_i^0, V_{Ti}^{1-}, V_{Ti}^0 and V_O^0, the zero-pressure method converges more quickly. Fig. 4b shows the case for V_{Ti}^{4-} and V_{Ti}^{1-} to illustrate some of these trends. Although the convergence speed of the two methods varies with the charge state of the supercell, the differences are always within 0.1 eV for the $3 \times 3 \times 5$ supercells as shown in Fig. 4a. Thus we use the constant-volume method with $3 \times 3 \times 5$ supercells for all subsequent calculations.

3.4. Defect energetics

Based on the above discussion, we present defect formation energies as a function of the temperature, oxygen partial pressure and Fermi level calculated by Eq. (1) for the supercell size of $3 \times 3 \times 5$. The calculated DFE of 3.6 eV for the fully charged Frenkel pair (Ti_i^{4+} and V_{Ti}^{4-}) is ~0.8 eV lower than the experimentally derived values of 4.4 eV at ~1500 K [35]. Part of this difference might be due to intrinsic errors in the DFT/GGA approach or the exclusion of the vibrational free energy, which was estimated by molecular dynamic calculations to account for around 5% of the DFE at 700 K in a Schottky defective supercell [11]. In this paper we are interested in the general trends predicted from the calculations rather than the absolute values, thus we continute to neglect this contribution, although it, in principle, could be obtained by computationally expensive, DFT-based phonon calculations. Table 3 lists the DFEs of Frenkel pairs and Schottky defects calculated by summing the DFEs of single defects, as well as their comparison with the experimental values [35,36]. It indicates that the fully charged pairs are most favorable

Table 3
The DFE of differently charged Frenkel and Schottky pairs compared with experimental values. The calculated pair energies are the direct summation of the individual DFEs calculated using Eq. (1) thus does not include the association energy between the individual defects, which agrees with the experimental condition of dilute solution in Refs. [2,35,36].

$Ti_i^{q+} + V_{Ti}^{q-}$	$DFE_{dV}^{Frenkel}$ (eV)	$DFE_{Exp}^{Frenkel}$ (eV)	$V_{Ti}^{2q-} + 2V_O^{q+}$	$DFE_{dV}^{Schottky}$ (eV)	$DFE_{Exp}^{Schottky}$ (eV)
$q = 4$	3.594	4.4–4.7 [2,35] and ⩽5.0 [36] for $q = 4$	$q = 2$	4.43	⩽6.6 [36] for $q = 2$
$q = 3$	5.494		$q = 1$	8.28	
$q = 2$	7.452		$q = 0$	12.42	
$q = 1$	9.491				
$q = 0$	11.590				

energetically and have energies closest to the experimental values.

By fixing T and P_{O_2}, the DFEs as a function of Fermi level can be considered, as illustrated in Fig. 5, where the Fermi level is referenced relative to the VBM. The fully charged defects at nearly all T and P_{O_2} combinations are more likely to occur, while the partially charged defects are rarely preferred. However, there is a sharp transition from the fully charged defects to the neutral defects at around 1.9 eV for the titanium interstitial and the oxygen

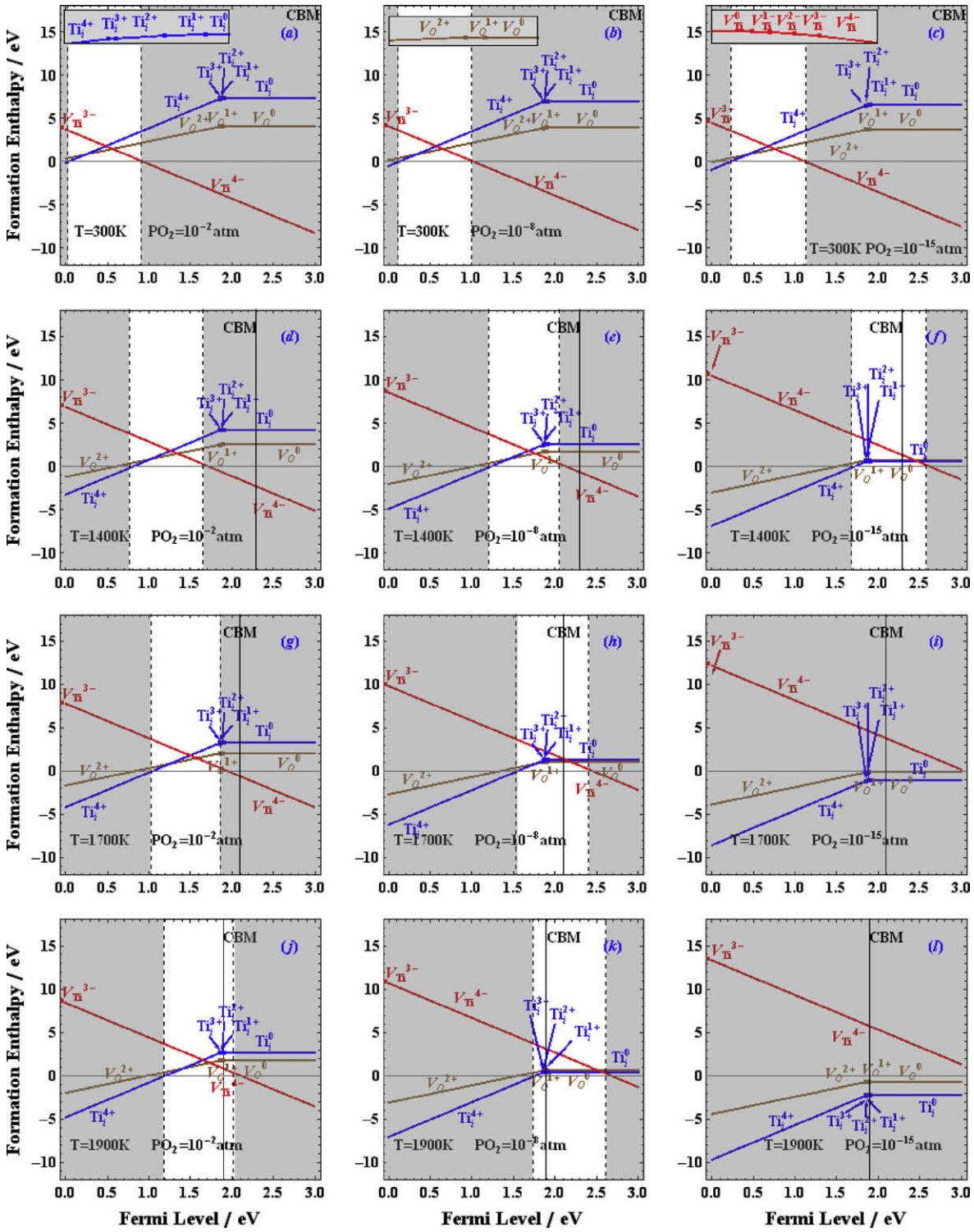

Fig. 5. DFE as a function of Fermi level at different T and P_{O_2}. The gray areas are forbidden by the charge neutrality condition. CBM is labeled for its experimental values at different temperatures; at 300 K it is at 3 eV. The insets in plots (a)–(c) enlarge the transition regions for each type of defect, respectively, which shows that the transition levels are ordered. The transition regions of titanium vacancies are cut off by the zero value of Fermi level or the valance band maximum, and thus most of them are not seen except for V_{Ti}^{3-} and V_{Ti}^{4-}.

Table 4
Total-energy differences between successive charge states of titanium interstitial defective supercells show the equal energy difference phenomenon.

$[\alpha]^q$	E_α (eV)	$E_\alpha^{q-1} - E_\alpha^q$ (eV)	$E_\alpha^{q-1} - E_\alpha^q - E_{VBM} - \Delta V$ (eV)
Ti_i^{4+}	−2456.23	5.38	1.854
Ti_i^{3+}	−2450.85	5.38	1.858
Ti_i^{2+}	−2445.47	5.42	1.885
Ti_i^{1+}	−2440.05	5.44	1.907
Ti_i^{0}	−2434.61		

vacancy, where all the defect transition levels shrink to a very narrow energy range, as indicated in Table 4. The close total-energy differences between any two supercells with successive charge states are a result of the fact that the differences in the charge distributions of the supercells are similar. In addition, when one electron is added to a Ti_i^{q-1} supercell to form a Ti_i^q supercell, the way that the added charge density distributes is insensitive to the original charge state, $q-1$. There is no direct evidence of switching of orders or the so-called negative-U effect [37] as the charge state varies.

Further examination of Fig. 5 reveals that the region where the dominant point defect has a negative DFE (the gray areas in the figure) is a forbidden region for the pure rutile TiO_{2-x} bulk material. This is because the P_{O_2}, T and Fermi level are not independent variables, but are constrained by the electroneutrality condition. At any given T and P_{O_2}, if the Fermi level were to be in the forbidden region, then the formation of a large concentration of the defect would change the Fermi level of the material drastically, which would then drag the Fermi level back to the allowed regions of Fig. 5. It is important to note that we are not referring here to a doped material in which the Fermi energy can be adjusted by a suitable choice of dopant, but rather to the intrinsic regime in which the Fermi energy must in principle be self-consistently determined by the intrinsic point defects that are in equilibrium at the given P_{O_2} and T.

Examination of Fig. 5 reveals several important trends. First, at high temperature and low P_{O_2}, such as in Fig. 5f, the allowed region for the Fermi level is close to the conduction band minimum (CBM), implying the stabilization of n-type TiO_2. By contrast, at low T and high P_{O_2}, such as in Fig. 5a, the allowed region for the Fermi level is closer to the VBM, implying the stabilization of p-type TiO_2. Additionally, Fig. 5i and 5l correspond to a combination of T and P_{O_2} for which rutile TiO_2 is not stable because all the dominant point defects have negative formation energies for all possible Fermi levels within the band gap; thus the forbidden region extends across the entire band gap. This prediction is consistent with the experimental findings that at the combination of high T and low P_{O_2} illustrated in Fig. 5i rutile transforms into two-dimensional (2-D) Magneli defect phases [1,38]. Thus, in general, increasing T or decreasing P_{O_2} will move the allowed region of the Fermi levels toward the CBM, while decreasing T or increasing P_{O_2} has the opposite effect. If we apply the

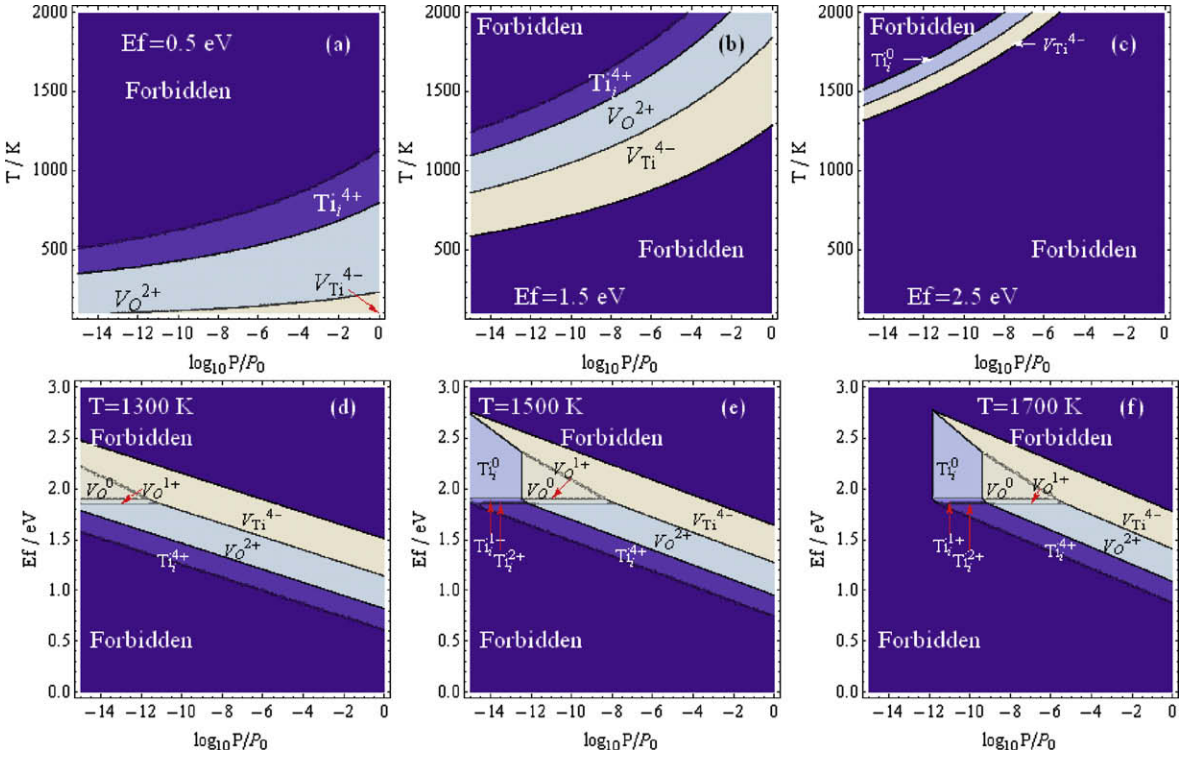

Fig. 6. Dominant point defect distribution in the 2-D phase space, showing (a)–(c) influence of the Fermi level (E_f) on the T–P behavior, and (d)–(f) the effect of temperature over the range of 1300–1700 K on the T–E_f behavior.

experimental finding that at around 1700 K $Ti_i^{4+}$is dominant, we conclude from Fig. 5g that the Fermi level in the allowed region is slightly above 1 eV, while in Fig. 5h it is slightly above 1.5 eV. When we take into account the experimental CBM [35] it is clear that n-type TiO_2 is predicted to be stable under these conditions.

It is also natural to plot the 2-D dominant defect phase diagrams in the P_{O_2} –T or the E_f–P_{O_2} phase spaces, as illustrated in Fig. 6. In the allowed regions the fully charged defects always occupy the largest phase space. Another evident trend is that when the Fermi level moves from the VBM to CBM, the corresponding temperature of the allowed regions in these 2-D phase diagrams increases and the stability range becomes narrower.

It is important to note that these results are quantitatively and sometimes qualitatively different from those in our previous publication [11]. Most notably, with the improved correction scheme in this paper, we find that the fully charged defects dominate over a significantly larger phase space. Thus, as we discussed in Section 3.2, the $2 \times 2 \times 3$ supercells with the Leslie–Gillan or Makov–Payne correction in Ref. [11] were not adequately converged.

As a final point, we should emphasize that the point defect formation energies presented here are in the dilute solution approximation and do not account for any defect associations, which may certainly occur in real systems. Defect associations would be expected to change the formation energies of the defect pairs depending on different conditions.

4. Conclusions

A combination of DFT and thermodynamic calculations is used to determine the defect formation energies in rutile TiO_2 as a function of T, P_{O_2} and Fermi level. The methods for correcting the artificial electrostatic interaction between the image defects caused by the supercell approximation in the DFT calculations are carefully examined and compared based on the analysis of the charge localization and the supercell size convergence behavior.

We find from the results of Bader charge density analysis that the Ti interstitial, like the Ti ion in the bulk, always carries close to a + 2 charge. In the cases where we create interstitials in supercells of other net charge, the charge difference is distributed over the neighboring ions. The charge density oscillates somewhat, corresponding to oscillatory relaxation of the ionic positions around the defect. Only in the case of Ti_i^{1+} does the excess charge appear to extend over a region contained within our largest supercell, and even in this case the charge transfers to the outer regions of the supercell are clearly constrained by its size. We find that the defect charge state is only well-defined relatively far from the defect site, and that charge density oscillations occur and eventually damp out. We also find that the ΔV correction is a more suitable correction method for the TiO_2 system than the previously utilized Leslie–Gillan or Makov–Payne correction [11]. We estimate that the errors due to elastic interactions of point defects with the supercell boundaries to be less than 0.2 eV in the present calculations.

From the calculated defect energies we construct point defect phase diagrams as a function of T, P_{O_2} and Fermi level, and show that fully charged defects dominate under most conditions. The calculated formation energy of a Frenkel pair of 3.6 eV agrees with the experimental value of 4.4 eV at ~1500 K reasonably well. We suggest that the 0.8 eV energy difference can be attributed, in part, to neglecting the vibrational energy in our current treatment and possibly to intrinsic errors in the DFT/GGA method. Analysis of the forbidden regions of these phase diagrams reveals the conditions of T, P_{O_2} and Fermi level under which the crystal structure of TiO_2 becomes energetically unstable. The predicted conditions are consistent with the experimental conditions that lead to the formation of Magneli defect phases. The results also suggest n-type TiO_2 at high T and low P_{O_2}, and p-type TiO_2 at low T and high P_{O_2}, in accordance with experimental data.

Acknowledgments

The authors acknowledge the support of the National Science Foundation through grants DMR-0303279 and DMR-0426870, and through TeraGrid resources provided by NCSA (TG-DMR-080029N).

References

[1] Baumard JF, Panis D, Ruffier D. Revue Int Hautes Temp Refract 1975;12:321.
[2] Baumard JF, Tani E. J Chem Phys 1977;67:857.
[3] Nowotny MK, Bak T, Nowotny J. J Phys Chem B 2006;110:16270.
[4] Lee DK, Jeon JL, Kim MH, Choi W, Yoo HI. J Solid State Chem 2005;178:185.
[5] Blumenth RN, Baukus J, Hirthe WM. J Electrochem Soc 1967;114:172.
[6] Balachandran U, Eror NG. J Mater Sci 1988;23:2676.
[7] Lee DK, Yoo HI. Solid State Ionics 2006;177:1.
[8] Zheng JX, Ceder G, Maxisch T, Chim WK, Choi WK. Phys Rev B 2007:75.
[9] Kohan AF, Ceder G, Morgan D, Van de Walle CG. Phys Rev B 2000;61:15019.
[10] Cho E, Han S, Ahn HS, Lee KR, Kim SK, Hwang CS. Phys Rev B 2006:73.
[11] He J, Behera RK, Finnis MW, Li X, Dickey EC, Phillpot SR, et al. Acta Mater 2007;55:4325.
[12] Makov G, Payne MC. Phys Rev B 1995;51:4014.
[13] Leslie M, Gillan MJ. J Phys C-Solid State Phys 1985;18:973.
[14] Baldereschi A, Baroni S, Resta R. Phys Rev Lett 1988;61:734.
[15] Zheng JX, Ceder G, Maxisch T, Chim WK, Choi WK. Phys Rev B 2006;73:104101.
[16] Kresse G, Furthmuller J. Phys Rev B 1996;54:11169.
[17] Kresse G, Joubert D. Phys Rev B 1999;59:1758.
[18] Perdew JP, Burke K, Ernzerhof M. Phys Rev Lett 1996;77:3865.
[19] Blochl PE. Phys Rev B 1994;50:17953.
[20] Van de Walle CG, Neugebauer J. J Appl Phys 2004;95:3851.
[21] Zhang SB, Northrup JE. Phys Rev Lett 1991;67:2339.
[22] Batyrev I, Alavi A, Finnis MW. Faraday Discuss 1999;114:33.
[23] Lozovoi AT, Alavi A, Finnis MW. Comput Phys Commun 2001;137:174.

[24] Liborio L, Harrison N. Phys Rev B 2008;77:104104.
[25] <http://www.webbook.nist.gov/chemistry/>.
[26] Finnis MW, Lozovoi AY, Alavi A. Annu Rev Mater Res 2005;35:167.
[27] Bader RFW. Atoms in molecules: a quantum theory. Oxford: Clarendon Press; 1990.
[28] Parker RA. Phys Rev 1961;1:1719.
[29] Binks JH, Duffy JA. J Chem Soc – Faraday Trans II 1985;81:473.
[30] Martin RM. Electronic structure: basic theory and practical methods. Cambridge: Cambridge University Press; 2004.
[31] Raebiger H, Lany S, Zunger A. Nature 2008;453:763.
[32] Castleton CWM, Hoglund A, Mirbt S. Phys Rev B 2006;73:035215.
[33] Freysoldt C, Neugebauer J, Van de Walle CG. Phys Rev Lett 2009:102.
[34] Zhu J, Yu JX, Wang YJ, Chen XR, Jing FQ. Chin Phys B 2008;17:2216.
[35] Smyth DM. The defect chemistry of metal oxides. Oxford: Oxford University Press; 2000.
[36] Ikeda JAS, Chiang YM, Garrattreed AJ, Vandersande JB. J Am Ceram Soc 1993;76:2447.
[37] Anderson PW. Phys Rev Lett 1975;34:953.
[38] Jacob KT, Hoque SM, Waseda Y. Mater Trans JIM 2000;41:681.